Radiation and surface wetness drive carbon monoxide fluxes from an Arctic peatland

Asta Laasonen[1], Alexander Buzacott[1], Kukka-Maaria Kohonen[1,2], Erik Lundin[3], Alexander Meire[3], Mari Pihlatie[4, 5], and Ivan Mammarella[1]

[1]Institute for Atmospheric and Earth System Research (INAR)/ Physics, Faculty of Science, University of Helsinki, Finland
[2]Department of Environmental Systems Science, ETH Zurich, Zurich, Switzerland
[3]Swedish Polar Research Secretariat, Abisko Scientific Research Station, Abisko, Sweden
[4]Department of Agricultural Sciences, Faculty of Agriculture and Forestry, University of Helsinki, Finland
[5]Institute for Atmospheric and Earth System Research (INAR) / Agricultural and Forest Sciences, University of Helsinki, Finland

Correspondence: Asta Laasonen (asta.laasonen@helsinki.fi)

Abstract. Carbon monoxide (CO) is an important trace gas in the atmosphere. However, its sinks and sources in terrestrial ecosystems remain poorly quantified. Understanding the terrestrial sink and source dynamics is crucial for better assessing the global CO budget. In this study, we investigated CO exchange in an Arctic peatland in northern Sweden to quantify the magnitude and key drivers of fluxes at the site. We measured CO fluxes using the eddy covariance method from August 2022 to September 2024. The study site was characterized by a heterogeneous surface structure with elevated dry palsas surrounded by wetter areas of bog. We found that the peatland was a net CO source during the measurement period, with fluxes ranging from –0.29 to 0.34 nmol m^{-2} s^{-1} (25th and 75th percentiles). The fluxes showed a systematic diurnal cycle, with daytime emission and nighttime uptake. Emissions were mainly driven by radiation, suggesting photo-driven production. Soil uptake was dependent on surface wetness, with higher consumption occurring in the dry parts of the peatland, suggesting that oxic conditions may favor CO uptake. ~~The annual cumulative CO flux for~~ We estimated by modeling that annual CO fluxes from the dry parts of the peatland ~~was estimated to be -44 mg CO m^{-2} yr^{-1} in 2022~~were ~~–2023 and -52~~ 43.3 and –32.2 mg CO m^{-2} yr^{-1} ~~in 2023–2024, while the flux for the wet parts of the peatland was 93~~ , and from the wet parts were 70.8 and 71.3 mg CO m^{-2} yr^{-1} in 2022–2023 and ~~84 mg CO m^{-2} yr^{-1} in~~ 2023–~~2024.~~ 2024, respectively. Despite the relatively small amount of CO released from the peatland, our study suggests that current global models may underestimate the CO source from northern wetlands.

1 Introduction

Carbon monoxide (CO) is an indirect greenhouse gas that plays a significant role in atmospheric chemistry by influencing tropospheric oxidative capacity. In the troposphere, CO is oxidized by hydroxyl radicals (OH), which are a key oxidant for various chemical species, including methane and other hydrocarbons. The oxidation of CO by OH accounts for 40% of OH removal, thereby reducing the oxidative capacity available for other trace gases and prolonging their atmospheric lifetime (Daniel and Solomon, 1998; Lelieveld et al., 2016). Most CO is emitted directly from anthropogenic sources or is formed by

the atmospheric oxidation of methane and other volatile organic compounds (VOCs), but natural systems are also known to release and consume CO (Liu et al., 2018; Zheng et al., 2019). However, the magnitude of CO sinks and sources in terrestrial ecosystems is poorly quantified.

Terrestrial ecosystems can act as net sources or sinks of CO, depending on the relative contributions of emissions from vegetation and soil production and consumption. CO production from vegetation and soil is ~~related to abiotic processes~~ commonly considered to result from abiotic processes, in which organic matter, litter, or plant material are degraded by radiation or temperature (Tarr et al., 1995; Derendorp et al., 2011; Lee et al., 2012; Bruhn et al., 2013; Fraser et al., 2015; Van Asperen et al., 2015). However, biological CO production from plants has also been reported (Wang and Liao, 2016). Soil consumption is a microbial process (Ragsdale, 2004; King and Weber, 2007), found to depend on soil carbon content (Inman et al., 1971; Moxley and Smith, 1998), soil water content (SWC) (King, 1999), and temperature (Whalen and Reeburgh, 2001). Soil consumption can occur under aerobic and anaerobic conditions, but with lower rates under anaerobic conditions (Conrad and Seiler, 1980). The exact chemical pathways of both CO production and consumption remain relatively unknown.

Terrestrial CO exchange has been studied using chamber measurements ~~(King, 2000; Kisselle et al., 2002; Varella et al., 2004; Bruhn et a~~ (King, 2000; Kisselle et al., 2002; Varella et al., 2004; Bruhn et al., 2013; Van Asperen et al., 2015; Sun et al., 2018; Muller et al., 2025) and the flux gradient method (Constant et al., 2008; van Asperen et al., 2024) across various ecosystems and climate regions. However, there is a lack of continuous and year-round measurements, which has recently been addressed by the eddy covariance (EC) technique (Pihlatie et al., 2016; Cowan et al., 2018; Murphy et al., 2023). The EC technique provides direct and continuous ecosystem-scale gas exchange measurements with high temporal resolution and minimal disturbance to the ecosystem (Aubinet et al., 2012), which allows the quantification of temporal variability and flux drivers of CO exchange at the ecosystem level.

To our knowledge, no CO flux studies have been conducted on terrestrial ecosystems in the Arctic region. Global modeling studies suggest relatively low biogenic production (Potter et al., 1996; Guenther et al., 2012) and soil consumption (Liu et al., 2018) in this region due to the cold climate. However, biogenic CO sources may play a significant role in high-latitude atmospheric chemistry since anthropogenic sources are limited. Existing global chemistry and climate models have been found to underestimate the observed CO concentrations at northern high latitudes, indicating that CO sinks are overestimated or CO sources are underestimated in this region (Stein et al., 2014; Szopa et al., 2021). To improve our understanding of the CO budget, the contribution of terrestrial ecosystems must be more accurately quantified in the Arctic region.

The aim of this study was to assess the contribution of biogenic CO fluxes in an Arctic peatland. We present a two-year time series of CO fluxes, covering both the vegetative and snow-covered periods, measured by the EC technique. We examined the seasonal and diurnal variations in fluxes to quantify the magnitude of CO exchange and to identify the primary meteorological and environmental variables driving CO fluxes. In addition, we estimated the CO fluxes from two different surface types, dry and wet, to investigate the possible differences in CO fluxes due to the surface heterogeneity. The measurements were conducted at Stordalen peatland in Abisko, northern Sweden, from August 2022 to September 2024.

2 Materials and methods

2.1 Study site

The study site, Stordalen peatland (68°21'20.8"N, 19°02'42.1"E, 360 m.a.s.l.), is located in the Arctic climate region in Abisko, northern Sweden. This region is characterized by long winters and relatively short summers. The mean annual temperature and ~~accumulated~~ the mean annual precipitation (1991–2020) for the area were 0.5°C and 347 mm, respectively (SMHI, 2024). The site is classified as a palsa bog with mostly ombrotrophic conditions, which makes it a nutrient-poor peatland. The surface structure of the study site is influenced by microtopography and ~~soil water content~~SWC. It is characterized by elevated dry palsas surrounded by wetter areas of bog. Permafrost is found within the palsas, and the degradation of permafrost has been observed in several parts of the peatland, leading to a slow transition of the palsas to wetter hollows (Malmer et al., 2005). The vegetation in the study area is classified into three main types based on the surface structure: shrub-dominated palsas (*Empetrum hermaphroditum*, *Rubus chamaemorus*, *Eriophorum vaginatum*, *Dicranum elongatum*, and *Sphagnum fuscum*), sphagnum- and cotton grass-dominated hollows (*Sphagnum balticum* and *Eriophorum angustifolium*), and sedge- and cotton grass-dominated hollows (*Carex rotundata* and *Eriophorum vaginatum*) (Malmer et al., 2005).

2.2 Eddy covariance fluxes

2.2.1 Flux measurements

EC measurements were conducted at a height of 2.2 m in the middle of the peatland from August 2022 to September ~~2024.~~ 2024 (Fig. 1). The location of the EC tower was selected to encompass both wet and dry surface types: wetter conditions were found to the southeast (SE) of the tower, while drier conditions were observed to the northwest (NW) of the tower.

Horizontal and vertical wind components were measured with the Gill HS-50 (Gill Instrument Ltd., England, UK) ultrasonic anemometer at a frequency of 10 Hz. The sonic anemometer~~was oriented~~ 's north was aligned 10° east relative to ~~the~~ geographic north. CO mixing ratios were measured using Aerodyne quantum cascade laser spectroscopy (QCLS: Aerodyne Research Inc., Billerica, MA, USA), which also simultaneously measured nitrous oxide (N_2O) and water vapor (H_2O) mixing ratios at a frequency of 10 Hz. The horizontal separation between ultrasonic anemometer and gas inlet was 0.19 m. The EC inlet was connected to the gas analyzer by a 30-m long tube with an inner diameter of 8.13 mm and an outer diameter of 12.0 mm. The gas analyzer pressure was set to 35 Torr and regulated by an electronic valve. The gas flow rate was approximately 16.2 L min^{-1}.

2.2.2 Flux processing

The EC data processing was performed using the EddyUH software (Mammarella et al., 2016), following the recommendations given in (Kohonen et al., 2020) for carbonyl sulfide flux processing. Fluxes were calculated as half-hourly averages, and linear detrending was used to separate the time series into mean and fluctuating components. The coordinate system was set using a 2D-coordinate rotation according to Kaimal and Finnigan (1994). Spikes were defined using a limit of the difference between

subsequent 10 Hz data points. If the difference between two data points exceeded 5 ppb for the CO mixing ratio and 5 ms^{-1} for the vertical wind velocity component, the data point was considered as a spike and replaced with the previous value. The time lag was determined by maximizing the cross-covariance between the CO mixing ratio and the vertical wind velocity component. Spectral corrections were applied to account for the low- and high-frequency attenuation of the covariance. High-frequency spectral corrections were made with an experimental approach (Aubinet et al., 1999). The low-frequency losses were corrected with a theoretical transfer function according to Rannik and Vesala (1999).

The measurements included a longer gap from February to April 2024 due to a broken scroll pump before its replacement. In addition, several shorter gaps occurred due to dirty inlet filters, power cuts, or other instrumentation problems, during which the flux measurements were not running. In total, the measurement period contained 24,212 calculated half-hourly fluxes, which were subsequently quality filtered. The calculated fluxes were accepted according to the following criteria: the second wind rotation angle was less than 10° in absolute value (removing 19 data points); the number of spikes in the 30-minute wind vertical velocity was less than 100 (removing 1,577 data points); kurtosis of the CO mixing ratio and vertical wind component was between 1 and 8 (removing 950 data points); skewness of the CO mixing ratio and vertical wind component was between –2 and 2 (removing 14 data points); and flux ~~stationary~~ stationarity was less than 0.3 (removing 8,981 data points). The low turbulent conditions were filtered out using a threshold value for friction velocity less than 0.1 ms^{-1} (removing 936 data points). In addition to these criteria, a few remaining spikes were filtered based on the standard deviation of ~~w~~ vertical wind velocity component larger than 2 ms^{-1} and CO mixing ratio larger than 9 ppb (removing 100 data points). Overall, the data coverage for the measurement period was ~~34%.~~ 31.7%. The data coverage across the different seasons is summarized in Table S1.

Finally, the relative contribution of the surface source area to the measured flux was calculated using the two-dimensional Flux Footprint Prediction (FFP) model (Kljun et al., 2015). We assumed a constant boundary layer height of 1000 m, because the model is insensitive to boundary layer height at low measurement heights, and estimated the roughness length to be 0.03 m based on the logarithmic wind profile in neutral atmospheric conditions. The other model parameters, including wind speed, wind direction, Monin-Obukhov length, standard deviation of lateral wind velocity component, and friction velocity, were obtained as output from the EC flux post-processing. The flux footprint was presented as 90% of the source area and was calculated for every half-hourly flux with a spatial resolution of 0.5 x 0.5 m.

2.3 Ancillary measurements

~~In addition to the flux data , other supporting measurements were~~ Ancillary data used in this study ~~. For the flux calculation, were obtained from the Integrated Carbon Observation System (ICOS) measurements (Lundin et al., 2023). These data include~~ relative humidity (RH), air pressure, ~~and~~ air temperature (~~Tair)were used. In the flux analysis, in addition to Tair,~~ Ta), photosynthetically active radiation (PAR), water table depth (WTD), soil temperature (~~Tsoil~~Ts), and ~~soil water content (SWC) at a~~ SWC at 10 cm depth~~(Tsoil) were also used. Tsoil and WTD are presented as an~~ . Ts and WTD represent the average of four measurement plots~~and SWC as an~~ , while SWC is based on the average of two measurement plots. ~~All data and the site description can be accessed from the~~ A detailed description of the ICOS instrumentation at the Stordalen peatland site

(SE-Sto), along with access to the ancillary dataset, is available through the ICOS Carbon Portal ~~database (Lundin et al., 2023)~~ (https://data.icos-cp.eu/portal/, last access: 10 July 2025).

2.4 Surface map

The surface cover map was created using drone imagery and a digital elevation model (DEM) (Abisko Scientific Research Station, 2025a, b). Elevated palsas were distinguished from wetter vegetation using a DEM threshold value of 383.0 m. Pixels with a DEM value higher than the threshold were classified as dry palsas, while pixels with a DEM value lower than the threshold were classified as wet hollows. The surface cover map was saved with a resolution of 0.5 x 0.5 m and was used together with the footprint analysis to calculate the contribution of dry and wet surfaces to the measured half-hourly fluxes.

2.5 Definition of seasons

We defined the seasons based on the calendar months: winter as December–February, spring as March–May, summer as June-August, and autumn as September–November. The beginning and end of the frozen period were determined according to Łakomiec et al. (2021), defined as days when the daily average peat temperature at 10 cm depth remained below/above 0°C for three consecutive days. The frozen periods during the measurement period were from 21 November 2022 to 11 May 2023 and 1 November 2023 to 12 May 2024.

2.6 Statistical analysis

2.6.1 Flux driver analysis

The flux drivers were analyzed using correlation analysis and a Random ~~Forest~~ forest (RF) model (sklearn.ensemble.RandomForestRegresso both performed on half-hourly values. The correlation between CO flux and meteorological and environmental variables was quantified using Spearman's rank correlation coefficients (scipy.stats.spearmanr). To assess the importance of ~~the variables~~ variables in linear regression, the Akaike Information Criterion (AIC) was used. ~~To interpret the RF model ,~~ The AIC is a metric used to compare the fit of different regression models, designed to identify the model that best balances goodness of fit and model complexity (i.e., the number of model parameters) (Akaike, 1973). The preferred model is the one with the lowest AIC value. In our case, this criterion was used to assess whether the added complexity of including temperature as a driver of CO flux is justified in addition to PAR.

To further investigate the drivers and detect potential nonmonotonic relationships not captured by simple linear analysis and Spearman's correlations, we applied SHAP (SHapley Additive exPlanations) values derived from an RF model. This approach allows for the identification of complex, nonlinear interactions that may not be captured by traditional linear methods or by Spearman's correlation. SHAP values were calculated using the SHAP library (https://shap.readthedocs.io/). The SHAP values provide a method to understand the factors driving the model's predictions by quantifying the marginal contribution of each feature to the output. ~~The statistical analysis in this section and following sections was performed with Python 3.12.17.~~

For the RF model, the data were split into a training (80%) and a validation (20%) set using a random split (random_split function). The hyperparameters— maximum depth (10, 12, 15, 20), number of estimators (50, 100, 150, 200), and minimum samples per leaf (2, 3, 4)— were optimized using a grid search function (sklearn.model_selection.GridSearchCV). The optimal model was selected by minimizing the mean ~~square~~ squared error (MSE). After cross-validation, the optimal model was refit using all available data and SHAP-values were calculated. The statistical analysis in this section and the following sections was performed with Python 3.12.

2.6.2 Parametrization of carbon monoxide fluxes

Two statistical models were developed to simulate the ~~30-minute~~ half-hourly CO fluxes and to assess the flux contributions from wet and dry surfaces. The first model was a simple linear model assuming a homogeneous surface structure and defined as:

$$F_{co} = \alpha * PAR + \beta\beta 1 * Ta + \beta 2 * Ta^2 + \gamma * PAR * Ta + \delta, \quad (1)$$

~~where α is the slope and β is the flux intercept.~~ The second model was a surface-type-specific model for heterogeneous surfaces and was defined as:

$$F_{co} = f_{dry} * (\alpha_{dry} * PAR F_{co,dry} + \beta_{dry}) + f_{wet} * (\alpha_{wet} * PAR + \beta_{wet}), F_{co,wet} \quad (2)$$

where $F_{co,dry}$ and $F_{co,wet}$ represent the contributions from dry and wet surface types, respectively. These components are defined as follows:

$$F_{co,dry} = f_{dry} * (\alpha_{dry} * PAR + \beta 1_{dry} * Ta + \beta 2_{dry} * Ta^2 + \gamma_{dry} * PAR * Ta + \delta_{dry}) \quad (3)$$

$$F_{co,wet} = f_{wet} * (\alpha_{wet} * PAR + \beta 1_{wet} * Ta + \beta 2_{wet} * Ta^2 + \gamma_{wet} * PAR * Ta + \delta_{wet}) \quad (4)$$

where f_{dry} and f_{wet} represent the footprint-weighted fraction of dry and wet areas, respectively, which were estimated from the surface map (Fig. 1). ~~The terms α_{dry}~~; α represents the sensitivity of CO fluxes to PAR; $\beta 1$ and ~~β_{dry} correspond to the slope and intercept for the dry surface, while α_{wet} and β_{wet} are the slope and intercept for the wet surface. The unknown~~ $\beta 1$ capture the linear and quadratic effects of Tair, respectively; γ represents the interaction between PAR and Tair, and δ is the intercept term.

The model parameters, α, β~~, α_{dry}, β_{dry}, α_{wet}, and β_{wet}~~ 1, $\beta 2$, γ, and δ were estimated using a Bayesian inference approach. Prior selection followed the methodology proposed by Buzacott et al. (2024) with two model runs. We used the first model run to estimate the probable parameters for each land use separately using the homogeneous surface type model (Eq. 1) and the second model run to estimate the probable parameters for mixed contributions from both surface types using the heterogeneous surface type model (Eq. 2).

For the first model run, all priors were assumed to follow uniform distributions (Table ~~S1~~S3). Data were divided into wet and dry classes based on the threshold of 70% of fluxes originating from wet or dry surfaces. In addition, the model parameters were estimated by assuming homogeneous surface structure, using all data for parameter estimation. The resulting posterior distributions were observed to follow approximately normal distributions (Fig. ~~S7).~~ S8). For the second run, all available data with mixed surface contributions were used. The prior distributions were defined based on the posterior information obtained from the first model run. All prior distributions were defined as normal distributions, based on the 95% confident interval of the posteriors from first model run, as suggested by Buzacott et al. (2024). The decision to use 95% confidence interval was made to ensure sufficient flexibility for the parameters under the mixed contribution. The priors for the second model run are presented in Table ~~S1.~~ S3 and the posterior distributions from the second run are shown in Fig. S9.

The model parameters were optimized numerically sampling using the Markov chain Monte Carlo (MCMC) method. The MCMC sampling was performed using pm.sample function from Python's PyMC library with 4 chains and 2000 samples in each chain, and tuning period 2000, in total 8000 samples. The output product from the MCMC sampling consisted of posterior probability distributions for each optimized model parameter. The model performance for both models was evaluated by comparing the predicted fluxes to the observed fluxes, using the root mean square error (RMSE) and the coefficient of determination (R^2) as performance metrics.

The models were initially ~~fit to all~~ fitted using data from March to November, excluding winter ~~data. Then~~ months. To investigate potential seasonal variability in the model parameters, separate analyses were subsequently conducted for each season (spring, summer, and autumn)~~to explore potential seasonal variability in the model parameters~~. An initial model using only PAR was tested, but Ta was added because it improved model performance (Table S2). The posterior parameter ~~sets from the second model run were~~ estimates from the final model were then used to simulate ~~the fluxes from~~ CO fluxes from both wet and dry ~~surfaces~~surface types. Annual estimates were ~~calculated as the cumulative sums of the simulated fluxes~~ derived by applying these posterior parameters to observed PAR and Ta data from March to November, under the assumption that wintertime fluxes were negligible and therefore set to zero.

3 Results

3.1 Environmental conditions and flux footprint

The mean annual temperature for the first measurement year (from August 2022 to August 2023) was 1.1°C, while the mean annual temperature for the second measurement year (from August 2023 to August 2024) was -0.1°C. The first year was warmer than the long-term average annual temperature (1991–2020), while the second year was colder than the long-term average (SMHI, 2024). The air temperature during the measurement period ranged from –38.8°C to 27.3°C~~, with~~ ; the minimum value was observed on 4 January 2024, and the maximum value on 22 July 2024. The soil temperature at a depth of 10 cm ranged from –12.2°C to 11.3°C, with the minimum recorded on 4 January 2024 and the maximum value observed on 22 July 2024. The total accumulated precipitation ~~for the first measurement year~~ was 325 mm ~~, and for the second measurement year , it was~~

in the first measurement year and 298 mm in the second year. In both years, annual precipitation was lower than the long-term average (1991–2020) for this region (SMHI, 2024). The daily mean PAR varied from 0.2 to 688.4 μmol $m^{-2}s^{-1}$, with the minimum value observed on 31 December 2022 and the maximum value on 1 July 2024.

The main wind directions during the study period were from the southeast (SE) and the northwest (NW), with 45% of the measured fluxes coming from the wind sector between 40~~0~~° and 180~~0~~° (SE) and 54% from the wind sector between 200~~0~~° and 350~~0~~° (NW). The distribution of wind directions was consistent across different seasons and stability classes (Fig. S1)~~.~~ , although slight day–night differences were observed during the non-frozen period, with SE winds more common at night and NW winds more frequent during the day (Fig. S2). The footprint-weighted average showed that fluxes from the NW wind direction were predominantly associated with the drier palsas, with 93% of the fluxes originated from the palsas and 7% of the fluxes originated from the wetter surface (Fig. 1). In contrast, fluxes from the SE direction were characterized by 23% originating from drier palsas and 77% from wetter surface.

3.2 Ecosystem scale fluxes

3.2.1 Flux timeseries

The ecosystem-scale half-hourly CO fluxes ranged from –0.29 to 0.34 nmol m^{-2} s^{-1} (25th and 75th percentiles), showing both net uptake and emission. The fluxes had strong seasonal variability, with the ~~highest emissions observed in summer and the highest uptake in autumn (Fig. 2). On a daily scale, the site acted~~ site acting as a net CO source ~~for most of the~~ in spring and summer ~~, with~~ (average median fluxes of 0.17 ~~nmol $m^{-2}s^{-1}$~~ and 0.24 nmol m^{-2} s^{-1}, respectively~~. In autumn, the site turned into~~), and as a net sink ~~for CO, with an average flux of~~ in autumn (–0.31 nmol m^{-2} s^{-1}~~.~~) (Fig. 2). The wintertime flux was minor (-0.09 nmol m^{-2} s^{-1}) compared to the fluxes of other seasons. ~~The pattern , where the site acted as CO source in spring and summer and CO sink in autumn~~ This seasonal pattern was consistent across both ~~measurement~~ years.

The CO flux showed a systematic diurnal cycle during the vegetative period, ~~but no such cycle was observed in the wintertime fluxes (Fig. 3). In spring and summer, emissions occurred during the daytime , while the consumption occurred during the nighttime (from 6 pm to 4 am), with the maximum emission observed at noon. The mean net CO flux was positive in both spring and summer, indicating that emissions dominated the net flux during these seasons. In contrast, autumn showed a negative mean flux, indicating that CO uptake predominated. The maximum mean daytime emission was highest in summer,~~ with daytime emissions and nighttime uptake. Emissions peaked at noon, reaching 1.11 nmol m^{-2} s^{-1} ~~at noon, while the minimum value observed at night was –0.33~~ in summer and 0.73 nmol m^{-2} s^{-1} ~~. In spring, the maximum mean emission was 0.73 nmol $m^{-2}s^{-1}$, and the minimum nighttime value was –0.14~~ in spring, while nighttime uptake was strongest in autumn (-0.44 nmol m^{-2} s^{-1}) (Fig. 3). In contrast, winter fluxes lacked a clear diurnal cycle. The diurnal pattern reflected seasonal differences, with net positive daily fluxes (emissions) in spring and summer, and net negative fluxes (uptake) in autumn. ~~In autumn, the net flux was negative, showing consumption at night and flux close to zero at noon, with maximum values of 0.01 nmol $m^{-2}s^{-1}$ and minimum values of –0.44 nmol $m^{-2}s^{-1}$.~~

3.2.2 Flux drivers

Seasonal and diurnal variations in CO fluxes were primarily driven by the seasonal and diurnal cycles of environmental conditions during the unfrozen period (Fig. 2). We found no significant correlation between wintertime fluxes and any environmental conditions (Fig. ~~S2~~S3) and thus wintertime fluxes were excluded from further analysis, with a focus on other seasons. Spearman rank correlations showed that PAR and temperature were the key factors explaining flux dynamics (Fig. 4). We found a positive correlation between half-hourly CO flux and both PAR (0.71) and ~~Tair~~ Ta (0.34), indicating that fluxes increase with higher radiation and warmer temperatures.

The ~~main drivers identified based on the correlation analysis , PAR and Tair were fitted against CO flux (Fig. 5). A linear correlation was observed~~ analysis revealed a strong linear relationship between CO flux and PAR ~~, while a nonlinear correlation was found with Tair. The linear regression for binned PAR had a~~ (R^2 = 0.996, p = 1.47e-8), with a regression slope of 0.0012 nmol m^{-2} s^{-1} and ~~an~~ intercept of –0.29 nmol m^{-2} s^{-1} ~~with an R^2 value of 0.996 and a p-value of 1.474e-8~~ (Fig. 5). The CO flux ~~was zero when PAR was~~ approached zero at approximately 250 μmol $m^{-2}s^{-1}$ ~~. This threshold value was also observed in the flux timeseries, where the site turned to net CO source in spring when PAR levels exceeded approximately 250 μmol $m^{-2}s^{-1}$ and autumn sink when PAR levels were below 250 μmol $m^{-2}s^{-1}$~~ PAR, a threshold that aligned with seasonal shifts in net CO flux observed in the time series (Fig. 2). ~~Due to positive correlation between PAR and Tair~~ A nonlinear relationship was found between the CO flux and TA (Fig. ~~4), we used the AIC to assess whether Tair could be an additional driver together with PAR. The AIC for using only PAR as an explanatory variable~~ 5, S4). Including TA in the linear ~~regression was 9014, while adding the Tair to the linear~~ model reduced the AIC ~~to 8836. This suggests that Tair~~ from 9014 (PAR only) to 8836, suggesting that Ta is also a ~~potential driver of CO flux, despite the multicollinearity between PAR and Tair~~significant explanatory variable for CO exchange.

According to Spearman's rank correlations, the correlation between CO flux and ~~Tsoil~~ Ts (0.12) was smaller than between the CO flux and ~~Tair~~ Ta (0.34) (Fig. 4). However, soil temperature played an important role, especially in spring and autumn flux dynamics, when the soil was frozen or unfrozen. The systematic soil consumption observed in the nighttime flux began in spring after the soil melted and ceased in autumn once the soil froze (Fig. 2). In the nighttime data, a higher negative correlation was found with ~~Tsoil~~ Ts (-0.41) than with ~~Tair~~ Ta (-0.28) (Fig. ~~S3~~S5). The correlation analysis including the daytime and nighttime fluxes did not reveal any clear relationship between the CO flux and f_{dry} (Fig. 4). However, in the nighttime fluxes, a negative correlation between CO flux and f_{dry} (-0.30) was observed (Fig. ~~S3~~S5).

~~To further investigate the drivers and detect potential nonmonotonic relationships not captured by simple linear analysis and Spearman's correlations, we applied SHAP values derived from an RF model. This approach allows for the identification of complex, nonlinear interactions that may not be captured by traditional linear methods or by Spearman's correlation.~~ The results from the SHAP values were consistent with the results of the Spearman correlations, with the highest positive fluxes associated with high PAR (Fig. 6). ~~Tsoil and Tair~~ Ts and Ta were found to be the second and the third most important drivers, with higher positive fluxes (emission) associated with low soil temperature and high air temperature. In the nighttime data, ~~Tsoil~~ Ts was the most important driver with the higher negative fluxes (uptake) associated with high soil temperature (Fig.

S4S6), consistent with Fig. 6. Additionally, SHAP values from both all data and nighttime data indicated that higher f_{dry} led to decreased fluxes, meaning that higher fluxes were observed in the wetter conditions (Fig. 6, Fig. S3S6). Figure S5 S7 presents partial dependence plots of SHAP values for each feature.

We analyzed the CO fluxes from the NW and SE footprints and found that fluxes from the NW footprint were consistently lower than those from the SE footprint throughout the study period (Fig. S6). Systematically lower net fluxes and nighttime fluxes were observed from NW footprint across all months, with the exception in April, when 7). On average, the net flux from the NW footprint was –0.03 nmol m^{-2} s^{-1}, whereas the net flux from the SE footprint showed a lower flux. The lower nighttime flux indicates that soil consumption in was 0.13 nmol m^{-2} s^{-1}. The nighttime flux from the NW footprint is higher was on average 2.1 times larger than in the SE footprint . The same was observed in SHAP analysis and correlation coefficients in nighttime data where the surface wetness was driving the ecosystem scale fluxes . (–0.23 nmol m^{-2} s^{-1} in NW vs. –0.11 nmol m^{-2} s^{-1} in SE). For example, in July, the mean nighttime flux from the NW footprint was –0.27 nmol m^{-2} s^{-1}, compared to –0.14 nmol m^{-2} s^{-1} from the SE footprint. This pattern was observed across all months, with the exception of April when the SE footprint exhibited slightly lower fluxes (0.05 nmol m^{-2} s^{-1} in NW vs. 0.02 nmol m^{-2} s^{-1} in SE). The consistently lower nighttime fluxes from the NW footprint suggest greater CO uptake by the soil in this area compared to the SE footprint.

3.3 Estimate of fluxes from dry and wet surface using Bayesian inference

3.3.1 Parameter distributions and model performance

We estimated the wet and dry fluxes numerically using a Bayesian inference approach with two model runs. The first model run used a threshold of 70% to separate the wet and dry fluxes and in the second model run the mixed contributions of fluxes were considered. The posterior parameter distributions from the first run are presented in Fig. S7. The distributions of parametersα and β, and the residuals were found to be approximately normally distributed. The posterior parameters from the first run were used as priors for the second run by assuming a normal distribution for the priors. The posterior distributions from the second run are shown in Fig. 7. Overall, there was no significant difference between the posterior distributions of α and β between the two model runs.

Clear seasonal variations were observed in both model parameters, α and β, as well as differences between the two surface structures in both parameters Seasonal and surface-type-dependent variability was evident in the estimated model parameters, highlighting the influence of both environmental conditions and surface heterogeneity on CO exchange dynamics (Fig. 7S9). The strongest radiation response (α) was observed in summer with a stronger response on dry surfaces than on wet surfaces. The difference in radiation response was observed in summer but not in spring and autumnseasonal differences were less pronounced when Ta was included as an explanatory variable, compared to the model using only PAR, suggesting that part of the observed seasonality was explained by temperature. The intercept parameter (δ) exhibited clear seasonal patterns: values were higher compared to other seasons in spring (β) was less negative in spring than in summer and autumn, indicating lower soil uptake in spring, δ_{dry} = –0.125 nmol m^{-2} s^{-1} and δ_{wet} = –0.106 nmol m^{-2} s^{-1}), indicating reduced CO uptake when the soil was still frozen. The intercept was more negative remained frozen. In contrast, lower intercepts were observed in summer

(δ_{dry} = –0.572 nmol m^{-2} s^{-1} and δ_{wet} = –0.231 nmol m^{-2} s^{-1}) and autumn (δ_{dry} = –0.582 nmol m^{-2} s^{-1} and δ_{wet} = –0.175 nmol m^{-2} s^{-1}), reflecting enhanced uptake during warmer conditions. Across all seasons, the intercept was lower on dry surfaces than on wet surfaces, with the ~~difference in intercept observed in all seasons, but being the largest~~ largest differences occurring in summer and autumn. Seasonal and surface-dependent variations were also apparent in other model parameters; however, the interpretation is complicated by the collinearity between PAR and Ta, which may confound individual parameter estimates and limit the ability to isolate their respective effects.

Model performance was calculated using the posterior parameter sets from the second run and is presented in Table ~~S2~~S4. The RMSE between different models ranged from ~~0.33~~ 0.32 nmol m^{-2} s^{-1} to ~~0.40~~ 0.37 nmol m^{-2} s^{-1} and R^2 values ranged from ~~0.17 to 0.74~~0.20 to 0.77. Overall, the model performance was best in summer and poorest in autumn. The mean of the predicted values follows the 1:1 line, with no obvious bias towards high or low values (Fig. ~~S8~~S10). The model performance was slightly better in the heterogenous surface models compared to the homogeneous surface models, ~~though the difference was relatively small~~with an average RMSE improvement of approximately 0.015 nmol m^{-2} s^{-1} and R^2 increases of 0.042.

~~Posterior parameter distributions of the model parameters α and β after the second model run. The parameters for wet (turquoise) and dry (yellow) are estimated considering the mixed contributions from both wet and dry surfaces. Homogeneous parameters represents the parameters without considering surface structure (green).~~

3.3.2 Annual cumulative flux

We estimated the annual cumulative fluxes ~~using~~ applying the posterior parameters from ~~the second model run. The cumulative annual fluxes are shown in Fig. **??**. We found that when seasonality was not considered, the models estimated larger uptake compared to when seasonality in parameterization was included. For the final annual cumulative flux estimates, we used the seasonal parametrization~~our seasonal model to the PAR and Tair data from March to November (Fig. S9). The difference in annual fluxes between the seasonally parameterized and non-seasonally parameterized models was small (Fig. S11). However, as we observed seasonal variation in model parameters, we chose to use the seasonal model for calculating annual fluxes to better represent temporal dynamics. The annual cumulative flux for dry surfaces was ~~–44.0~~ –43.3 mg CO m^{-2} yr^{-1} in 2022–2023 and ~~–51.5~~ –32.2 mg CO mg CO m^{-2} yr^{-1} in 2023–2024, while for wet surfaces, it was ~~92.7~~ 70.8 mg CO m^{-2} yr^{-1} in 2022–2023 and ~~84.4~~ 71.3 mg CO m^{-2} yr^{-1} in 2023–2024. There was a significant difference between wet and dry surfaces, with dry surfaces acting as CO sinks and wet surfaces as CO sources. Interannual variability in annual cumulative fluxes was minor. The cumulative annual flux in the homogeneous model was ~~11.6~~ -0.03 mg CO m^{-2} yr^{-1} in 2022–2023 and ~~4.2~~ 11.4 mg CO m^{-2} yr^{-1} in 2023–2024. The confidence intervals and standard deviations of annual estimates are presented in Table ~~S3~~S5.

~~Probability distribution of cumulative annual fluxes in wet (turquoise), dry (yellow) surfaces and in homogeneous surface (green) (a) using seasonal parametrization and (b) using no seasonality in parametrization.~~

4 Discussion

4.1 ~~Ecosystem scale fluxes~~Flux magnitude and temporal variations

4.1.1 ~~Flux magnitude and temporal variations~~

Our results show that CO flux dynamics are influenced by the environmental conditions~~and~~ , particularly radiation and temperature, and vary according to the surface cover type. We found that the wet surfaces of the peatland emit CO, while the drier areas of the peatland act as CO sinks. This study provides new insights into the magnitude and drivers of biogenic CO fluxes in Arctic peatlands, contributing to a better understanding of the role of terrestrial ecosystems to the CO budget.

The CO fluxes reported in this study are similar in magnitude to the fluxes reported in previous EC flux studies in a boreal cropland and two temperate grasslands, with mean fluxes ranging from –1 to 2 nmol m^{-2} s^{-1} (Pihlatie et al., 2016; Cowan et al., 2018; Murphy et al., 2023). The modelled annual fluxes in this study ranged from –32 to 71 mg CO m^{-2} yr^{-1}. When compared with annual fluxes reported in other EC studies, particularly from temperate regions where values range from 360 to 880 mg CO m^{-2} yr^{-1} (Cowan et al., 2018; Murphy et al., 2023), our results indicate a lower contribution of biogenic CO emissions from Arctic peatlands relative to temperate grasslands.

Consistent with earlier studies, our results show clear seasonal variations in CO fluxes (Pihlatie et al., 2016; Cowan et al., 2018). The site acted as a net source of biogenic CO during the spring and summer, and a net sink during the autumn. The highest net emissions were observed in summer, although the difference between summer and spring was smaller than would be expected if fluxes were determined solely by radiation from living plants. Spring emissions began even before snowmelt and the onset of the growing season, suggesting that CO degradation from senescent plants and litter from the previous year may contribute to the emissions. This is also supported by other studies reporting that senescent plants and litter emit higher amounts of CO than living plants ~~(Derendorp et al., 2011; Lee et al., 2012)~~(Tarr et al., 1995; Derendorp et al., 2011; Lee et al., 2012). Early spring CO emissions were reported by Pihlatie et al. (2016) from reed canary grass, where high emissions were observed after snowmelt before the start of the crop growth. Another factor probably contributing to the relatively high net emissions in the spring was frozen soil, which results in significantly lower nighttime CO consumption compared to the summer and autumn periods.

The largest net CO consumption was observed during late summer and early autumn in the nighttime data. Nighttime was defined as periods when PAR was less than 1 μmol $m^{-2}s^{-1}$. In high latitudes, dark conditions during mid-summer are limited, and therefore we have only ~~a little~~ limited nighttime data available for the summer months. The summer diurnal plot (Fig. 3) includes the effects of radiation on fluxes during nighttime hours (7 pm to 4 am), when net uptake was observed, making it difficult to fully understand the development of soil uptake throughout the growing season. However, we observed that the highest net uptake occurred in late summer and autumn. We speculate that microbial communities responsible for CO consumption require time to develop (King and Weber, 2007; Cordero et al., 2019), which could ~~explains~~ explain the higher consumption in late summer and autumn, rather than in early or mid-summer. In autumn, when CO production ceases due to PAR limitation, consumption became more visible and was also observed in daytime fluxes. In August, both soil and air

temperature were higher than in September and October, suggesting that thermal production, in the absence of radiation, may influence the net flux and reduce CO consumption.

The importance of soil temperature as a driver for CO fluxes increased in autumn, when the site was mainly a net sink of CO. The transition from a net source to a net sink of CO occurred when PAR level dropped below 250 μmol $m^{-2}s^{-1}$. This shift from a net source to a net sink in autumn is a result of a decreased photoproduction of CO due to limited daytime radiation in high latitudes and may also indicate increased CO consumption in the soil. ~~Similar~~ A similar shift has also been observed in a boreal cropland (Pihlatie et al., 2016), but not in temperate ecosystems (Cowan et al., 2018; Murphy et al., 2023). The soil consumption in autumn continued until the soil froze.

The contribution of wintertime fluxes to the total CO flux was relatively small compared to fluxes observed in other seasons, likely due to both limited production and consumption. The lack of correlation between wintertime fluxes and environmental variables suggests minimal CO activity during winter, or at least no significant process that would result in a net flux different from zero. The limited daylight and snow cover may prevent CO emissions, while ~~the frozen soil likely ceased the CO consumption~~ CO consumption likely ceased due to frozen soil. Due to the small flux during the winter, this study focused primarily on spring, growing season, and autumn fluxes. ~~However, future studies should also give attention to wintertime fluxes as well.~~

4.2 Processes and flux drivers

We observed a systematic diurnal cycle, with daytime emissions peaking at noon and nighttime uptake, a pattern consistent with other studies (Pihlatie et al., 2016; Cowan et al., 2018). Daytime emissions followed the pattern of PAR, suggesting that the CO production is driven by radiation, likely due to photodegradation of organic matter, litter or living plants ~~(Tarr et al., 1995; Derendorp et al., 2011; King et al., 2012; Bruhn et al., 2013). The~~ (Tarr et al., 1995; Derendorp et al., 2011; King et al., 2012; Bruhn et al., 2013). Our flux driver analysis indicated that PAR is the primary factor driving ecosystem scale CO fluxes. ~~Unfortunately, using the EC technique, we cannot determine the exact source process of these emissions. However, the~~ The linear relationship between PAR and CO, also reported in Bruhn et al. (2013), suggests ~~towards an~~ an underlying abiotic process, with no obvious limiting biotic factors controlling the emissions.

~~Previous studies have reported both photoproduction (King et al., 2012; Bruhn et al., 2013; Fraser et al., 2015) and~~ However, thermal production (Lee et al., 2012; Van Asperen et al., 2015) ~~of~~ and biotic production of living plants (Wang and Liao, 2016) have also been reported as potential sources of CO at the ecosystem scale. For example, a recent study found that heat-controlled biogenic CO production from plants is linked to biotic processes rather than photoproduction (Muller et al., 2025). Unfortunately, using the EC technique, we cannot determine the exact source process of these emissions.

Our analysis indicates that air temperature is an important factor influencing CO ~~. In our analysis, we were unable to exclude the potential influence of air temperature on CO~~ exchange. Both AIC and SHAP values indicate that air temperature is a statistically significant driver, together with PAR, with higher emission observed at warmer temperatures. This was also supported by our residual analysis, which revealed a non-linear relationship in the flux residuals derived from the linear model of PAR (Fig. S4). Due to the correlation between temperature and radiation, it is challenging to fully disentangle their independent

effects on CO fluxes. We propose that photo- and thermal degradation may occur simultaneously. However, as the net nighttime CO fluxes were mostly negative, if thermal degradation does occur, it is likely much smaller than the observed nighttime CO consumption. The measured nighttime CO consumption is hence a net sum of microbial CO consumption and abiotic CO production via thermal degradation, both of which are likely driven by temperature. However, we cannot exclude the possibility of heat-controlled biotic sources contributing to CO fluxes (Muller et al., 2025).

According to our driver analysis, we were not able to identify relationships between environmental drivers and CO uptake as clearly as we did for CO emissions. We found that soil temperature was an important driver and CO uptake was observed only during the unfrozen periods. However, we did not find any clear relationship between soil temperature and CO flux during the unfrozen period. Several factors may explain this: during the daytime, net fluxes were primarily driven by ~~photoproduction~~radiation, and at nighttime, when CO uptake was observed, the data were limited due to low turbulent conditions and the lack of dark conditions in summer. As mentioned earlier, ~~both thermal production~~thermal production, which is the one potential source of CO and soil consumption are both likely driven by temperature, which may lead to similar responses for each process, thereby minimizing the changes observed in net flux (King, 2000).

In addition to temperature, SWC has been proposed as a potential driver of CO uptake. ~~with an optimal range of SWC . Very low SWC may reduce microbial activity, while very high SWC prevents~~ Low SWC can limit microbial processes, while high SWC may prevent gas diffusion in the soil (Moxley and Smith, 1998). However, we could not identify a clear relationship between CO flux and SWC, but we observed systematically lower fluxes from the drier footprint compared to the wetter footprint. This was seen in both daytime and nighttime data, as well as in SHAP values. The higher consumption observed in drier conditions suggests that CO ~~consumption~~ uptake is larger under oxic conditions than under anoxic conditions~~, which~~ . This is consistent with other studies~~(Funk et al., 1994; Rich and King, 1999).~~ , which have found that most CO consumption occurs under oxic conditions (Funk et al., 1994; Rich and King, 1999). This is expected, as CO is reactive and can be oxidized to CO_2 (Bartholomew and Alexander, 1979; King and Weber, 2007). It is also possible that in wet conditions, CO diffusion was prevented in the soil, as proposed in Moxley and Smith (1998). ~~A similar difference in fluxes between the NW and SE footprints in the Stordalen peatland was reported in Łakomiec et al. (2021), where they found that methane emissions were systematically lower in NW footprint than SE footprint.~~

4.3 Flux modeling

4.3.1 ~~Model parameters and annual flux~~

~~To simulate the fluxes from wet and dry surfaces, we used the linear relationship between CO flux and PAR~~We used the regression model to estimate CO fluxes from the dry and wet surfaces, and to calculate the annual fluxes from these two surfaces. The modeling ~~results indicated that the difference between wet and dry surfaces was pronounced in both slope and intercept. The higher radiation response on dry surfaces compared to wet surfaces suggests that dry surfaces emit more CO than wet surfaces. The difference in radiation response between wet and dry surfaces was observed in summer but not in~~ approach has its own limitations in terms of data coverage as well as the modeling approach. Our data coverage for the full measurement

period was 31.7%, which is relatively low but within the expected range for EC measurements for gases with low signal-to-noise ratio. In the data filtering, we followed standard quality control procedure (Mauder and Foken, 2006) with the most common reason for data exclusion being failure to meet the stationarity criterion. The limited data coverage causes uncertainty in the annual fluxes, especially during nighttime and spring and autumn seasons when fewer data points are available.

We observed seasonal variability in the model parameters (Fig. S9), and thus to reduce the potential seasonal bias caused by uneven data distribution, we applied seasonal parameterization in the model. However, the comparison between the seasonal and non-seasonal models showed no significant difference in annual flux estimates (Fig. 11), suggesting that the seasonal biases do not lead to major errors in the overall annual budgets.

It is important to note that the annual fluxes reported in this study are based on modeled estimates. The model performed well for the existing dataset and was used as a tool to estimate fluxes for both wet and dry surfaces. However, we did not test the model's predictive power on unseen data. In particular, the second-degree polynomial function used to represent the temperature response may not generalize well to other years or conditions. Furthermore, the use of this function during winter may lead to overestimation of fluxes at low temperatures, as the polynomial structure predicts emissions in cold conditions.

~~The difference in intercepts between wet and dry suggests that soil consumption differed between the two surfaces. Higher uptake was found in dry palsas during summer and autumn, but not during spring. The seasonality in intercepts supports the results of higher net uptake in late summer and autumn, as observed in the measurements.~~

The heterogeneous surface-structure models are found to perform better than homogeneous models in heterogeneous EC footprints (Ludwig et al., 2024; Tikkasalo et al., 2025). ~~However, we did not find significant difference in model performance between the heterogeneous and homogeneous models. In our case,~~ In our analysis, the heterogeneous model performed better than the homogeneous model, reducing RMSE 2.4–7.5%. The parameter distributions of the homogeneous model typically settled between the wet and dry parameter distributions, most often closer to the dry distributions. The reason that the homogeneous parameters were closer to the dry surface type is likely related to wind directions, which show a slight bias toward the NW (Fig. S1). If the wind direction distributions were more strongly biased toward a single wind direction, a larger difference in model performance between the heterogeneous and homogeneous models could be expected. We also found that the SE footprint contained a higher proportion of nighttime data compared to the NW footprint, which may introduce a potential bias in the model, as fluxes in the SE region could be underestimated due to the more lower turbulent conditions (Fig. S2). However, we consider the impact on our modeling approach and results is minimal.

~~Our analysis show that in Stordalen peatland the annual flux for wet surfaces is 76-85 mg CO m^{-2} yr^{-1} and the annual flux for palsas (dry surfaces) ranges from –52 to -44 mg CO m^{-2} yr^{-1}. When comparing our results to annual fluxes presented in other studies, the flux in temperate zone ranges from 360–880 mg CO m^{2} yr^{-1} (Cowan et al., 2018; Murphy et al., 2023), indicating a much higher contribution of biogenic CO emissions from temperate grasslands compared to arctic peatlands.~~

4.4 Future research

~~By comparing our results to the process-based CO model(Liu et al., 2018) we observe that our fluxes differ from the modeled fluxes. In the modeling, non-forested boreal wetlands are modeled as a small sink of CO (net flux: -0.18 Tg CO yr^{-1},~~

~~area $0.83*10^6$ km^2~~The Stordalen peatland has slowly transitioned from dry, permafrost dominated palsa areas to wetter, sedge dominated fens due to global warming (Varner et al., 2022). The land cover changes have been observed on decadal timescales (Varner et al., 2022). This is important also in terms of CO exchange, because in the future, we can expect increased surface wetness (more sedge- and open water-dominated vegetation), which ~~corresponds to an average annual flux of −261 mg CO m^{-2} yr^{-1} for non-forested boreal wetlands. Although the annual flux of CO from Stordalen peatland is relatively small, our study suggests that current process-based models incorrectly define wetlands as CO sinks instead of CO sources (Guenther et al., 2012; Liu et al., 2018)~~may also lead to higher CO emissions. To better understand the annual variability and future changes of CO fluxes, longer term measurements are needed.

4.4.1 ~~Limitations and uncertainties~~

~~Solving heterogeneous EC fluxes relies on an accurate surface cover map. In this study , we had only one drone image from early summer 2024, and thus we assumed that~~ In our two-year study period, we did not expect significant changes in the wet and dry ~~classes does not have significant seasonal changes.~~ surface classes at either seasonal or annual scale. This assumption is important, as accurately characterizing heterogenous EC fluxes, we need an accurate surface cover classification. The seasonality of surface wetness in ~~Stordalen mire~~ the Stordalen peatland was studied by Łakomiec et al. (2021) and they did not observe any significant seasonal changes in wet and dry classes. ~~We also assumed that the surface wetness does not have significant annual variations, which is likely true in short-time periods. In the long-term, however, the surface structure is slowly changing more wet due to the global warming, as permafrost thaws and palsas collapse.~~

~~In the modeling,~~ However, in the model, we assumed that the flux from each wet and dry pixel ~~contributes equally to the total flux~~had uniform responses within each area. In practice, this assumption may not be valid, as the vegetation within each surface class may not be completely homogeneous. Especially in the wet class, the surface structure is a mixture of open water areas, sedges, and mosses, which likely contribute differently to the flux. We can expect seasonal and annual variations in open water areas and sedge cover on the peatland, even though it does not directly affect our wet and dry classification. To better understand the contribution of different surface structures within the wet and dry classes, other methods, such as chamber measurements ~~,~~are needed.

~~We found that the model parameters showed seasonal variations, and to reduce the model uncertainty, we used seasonal parametrization. The developed models without seasonal parametrization did not perform well in early-spring conditions when the soil was frozen. Therefore, we calculated the annual fluxes by assuming winter fluxes to be zero and calculating the cumulative flux for March to November by parameterizing the model parameters for different seasons separately. Without this seasonal parametrization, the modeled cumulative fluxes overestimate the sinkin spring, when soil is frozen but emission occurs (Fig. 7).~~

~~The annual estimates for wet and dry presented in this study are based on the modeled values. In future studies,~~ Although the annual CO flux from the Stordalen peatland is relatively low, our findings suggest that current process-based models may inaccurately represent wetlands as CO sinks rather than sources (Guenther et al., 2012; Liu et al., 2018). When compared to the ~~cumulative annual flux for the gap-filled data should also be estimated. To~~ process-based CO model by Liu et al. (2018)

, our CO fluxes show a clear divergence. In that model, non-forested boreal wetlands are classified as a small CO sink, with an average annual flux of –217 mg CO m^{-2} yr^{-1}. In contrast, our results indicate that these ecosystems may act as net CO sources, emphasizing the need for further research to better understand the ~~annual~~ environmental drivers and variability of CO fluxes ~~, longer-term measurements are needed. In addition, in the annual estimates, we assumed that the wintertime flux is zero, which should be investigated futher in future studies~~at the ecosystem scale in high latitude wetlands.

5 Conclusions

~~As CO indirectly affects Earth's radiative balance, understanding the sinks and sources of atmospheric CO is crucial.~~ To interpret the role of wetlands in the global CO budget, we studied ecosystem-scale CO fluxes in Arctic peatlands. Our results revealed previously unknown biogenic sources of CO from northern peatlands to the atmosphere~~, which~~ . The reason that these sources were unknown is partly due to the lack of long-term measurements at the ecosystem level, but also ~~due to the lack of knowledge of~~ to an incomplete understanding of CO processes. We also report that CO flux magnitude depends on surface wetness with uptake from dry areas and emission from wet areas. This study ~~was limited to a single peatland and two years of data. Thus, to capture the annual variations and to obtain a broader understanding of CO flux dynamics in wetlands in response to changing climate, continuous, long-term measurements from multiple wetland sites are necessary. Despite these limitations, this study provides new data set~~ provides a new dataset valuable for modeling and new parametrization of current process-based CO models. Our study suggests that current global models may ~~underrestimate~~ underestimate the CO source from northern wetlands.

Code and data availability. The data and code used for the analyses are available on the author's GitHub (https://github.com/astatuulia/co_flux_SE-Sto). The meteorological data can be downloaded from the ICOS Carbon Portal database (https://www.icos-cp.eu, last access: 5 March 2025).

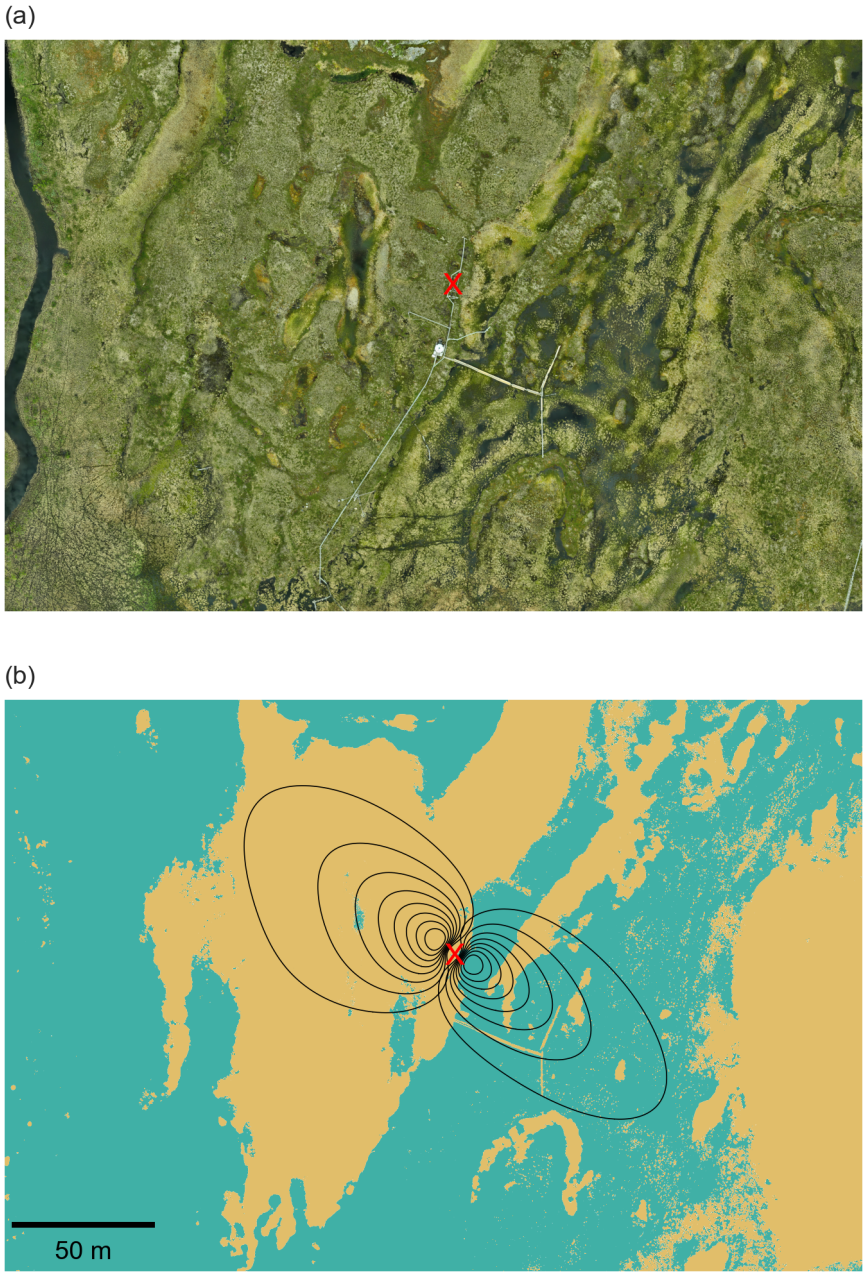

Figure 1. ~~The surface map~~ (a) Aerial drone image of the study site and (b) the surface map derived from the digital elevation map (DEM) and flux footprints in the northwest (NW) and southeast (SE) directions~~(a), the relative contribution of wet and dry surfaces in the NW footprint (b), and the SE footprint (c)~~. Black lines represent flux footprint contours from 10% to 80%, and the location of the EC tower is marked by a red cross. The yellow color indicates the dry surface and the turquoise color the wet surface.

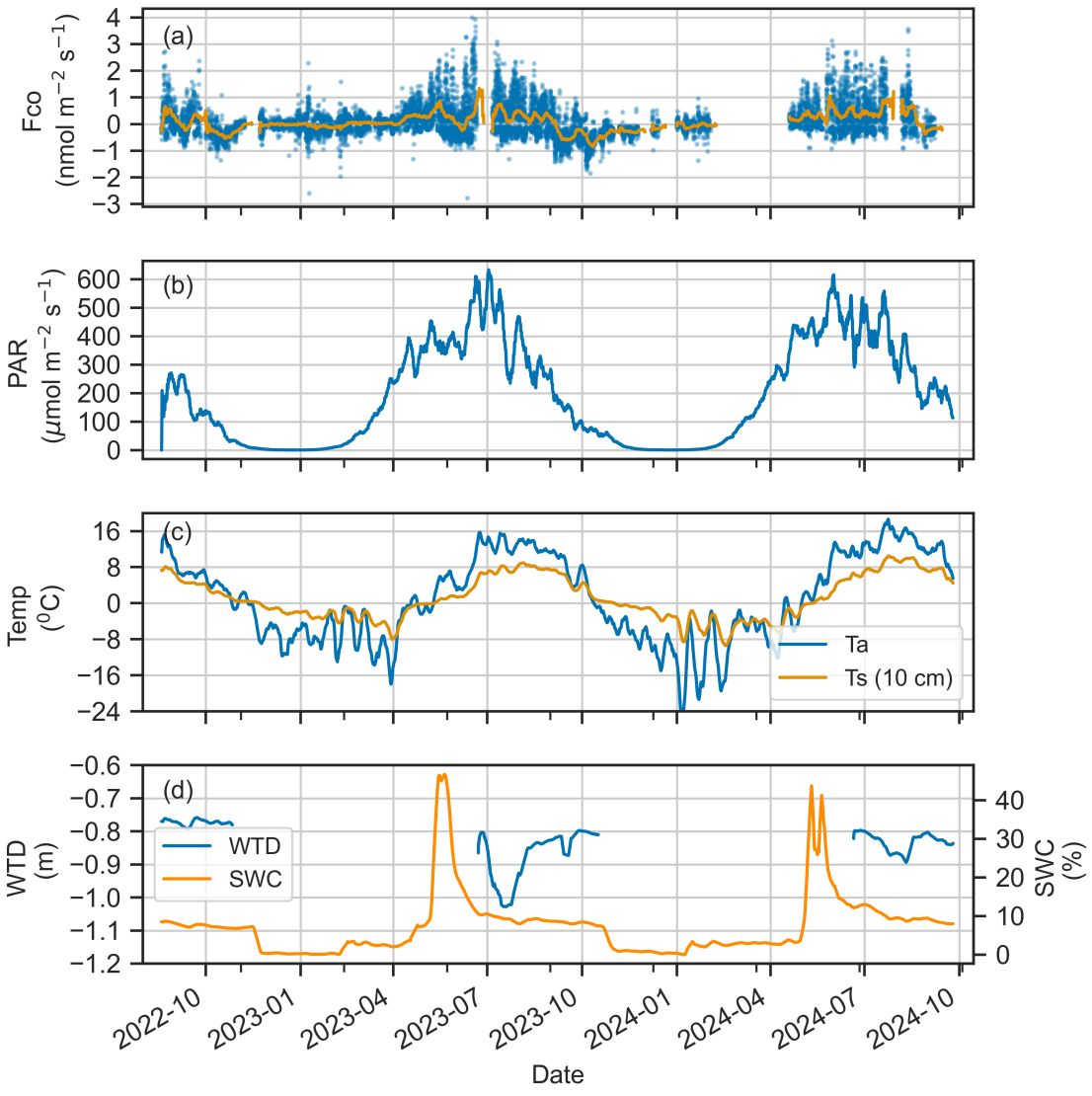

Figure 2. Timeseries of (a) CO flux, (b) photosynthetically active radiation (PAR), (c) air temperature (~~Tair~~Ta) and soil temperature at 10 cm depth (~~Tsoil~~Ts), and (d) water table depth (WTD) and soil water content at 10 cm depth (SWC). The solid line represents the 7-day rolling average (a-d) and the dots indicates half-hourly flux (a).

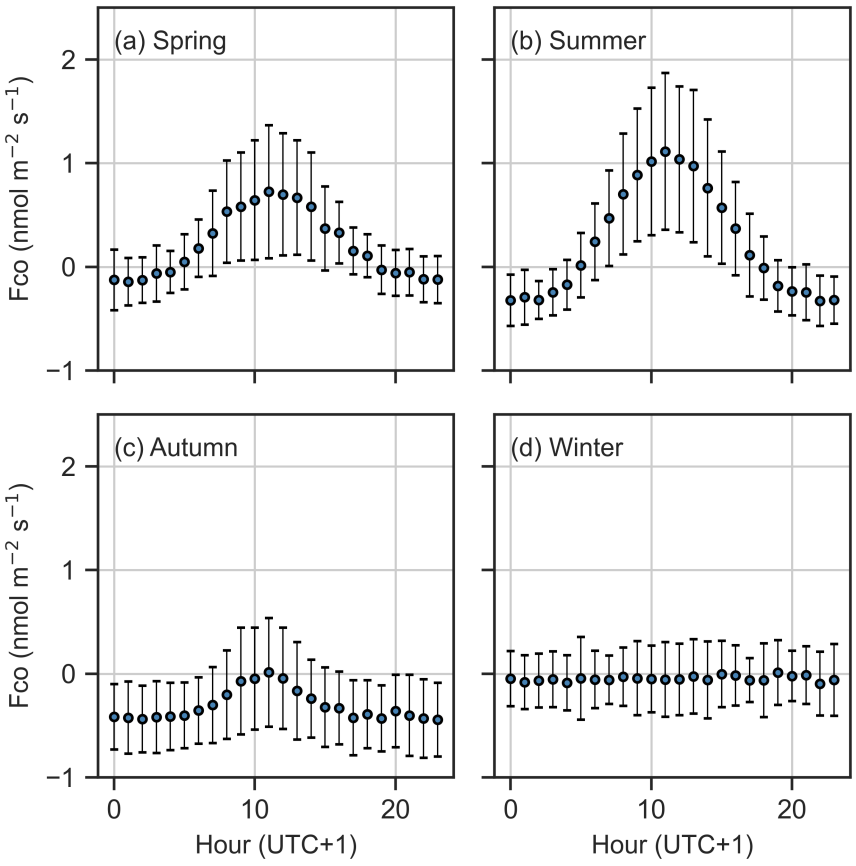

Figure 3. Diurnal cycle of CO flux (mean and standard deviation) in (a) spring, (b) summer, (c) autumn, and (d) winter.

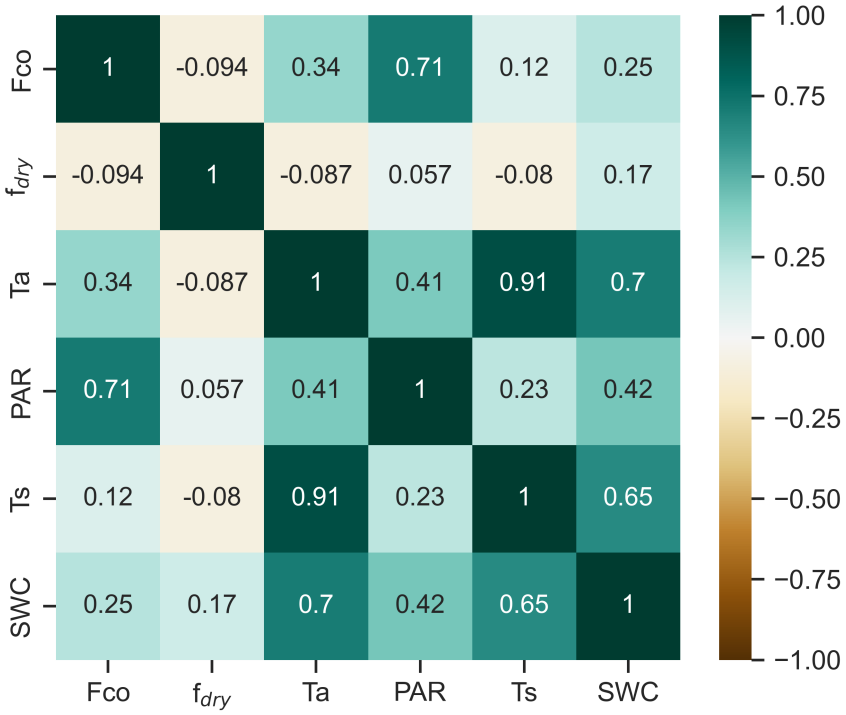

Figure 4. The correlation matrix of Spearman's rank correlation coefficients for CO flux (Fco) and flux drivers: soil temperature at a depth of 10 cm (~~Tsoil~~Ts), photosynthetically active radiation (PAR), air temperature (~~Tair~~Ta), and fraction of dry surface area (f_{dry}), calculated for half-hourly values during March–November.

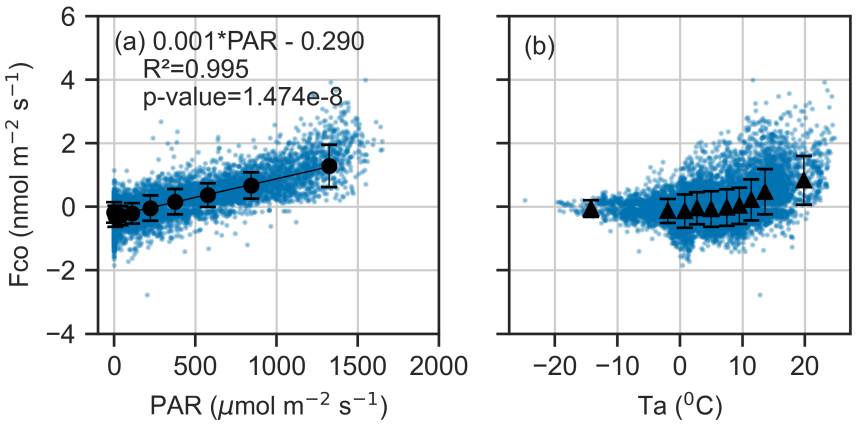

Figure 5. Binned mean and standard deviation between CO flux and (a) photosynthetically active radiation (PAR) and (b) air temperature (~~Tair~~Ta) during March–November. The data is divided in ten equal-sized bins and blue dots represent the 30-minute fluxes. A linear regression line is fitted to PAR.

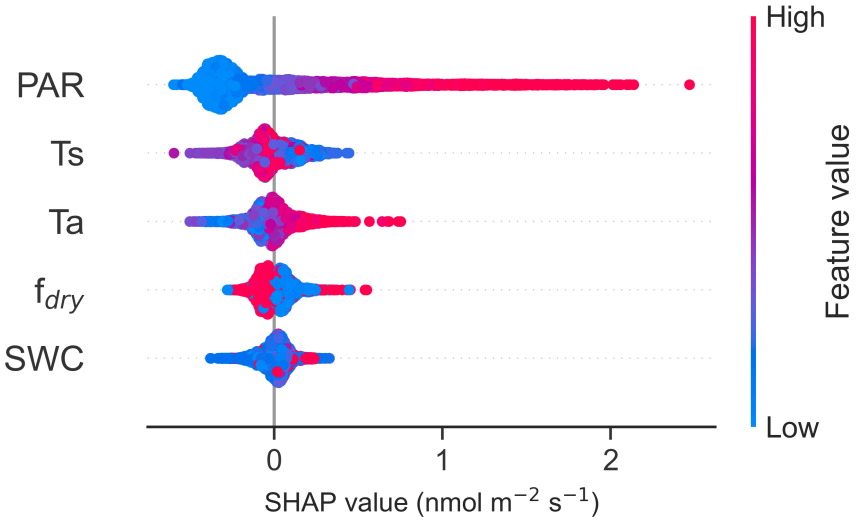

Figure 6. The SHAP (SHapley Additive exPlanations) values of the Random forest (RF) model for CO flux drivers photosynthetically active radiation (PAR), air temperature (~~Tair~~Ta), soil temperature at a depth of 10 cm (~~Tsoil~~Ts), soil water content at a depth of 10 cm (SWC), and fraction of dry surface area (f_{dry}). The SHAP values indicate the impact each feature has on the model output, with a negative value indicating a reduced flux and a positive value an increased flux. The blue color represents low feature values and red color high feature values. The zero line is the baseline (the average prediction). The SHAP values ~~are~~ were calculated using the data collected from March to November.

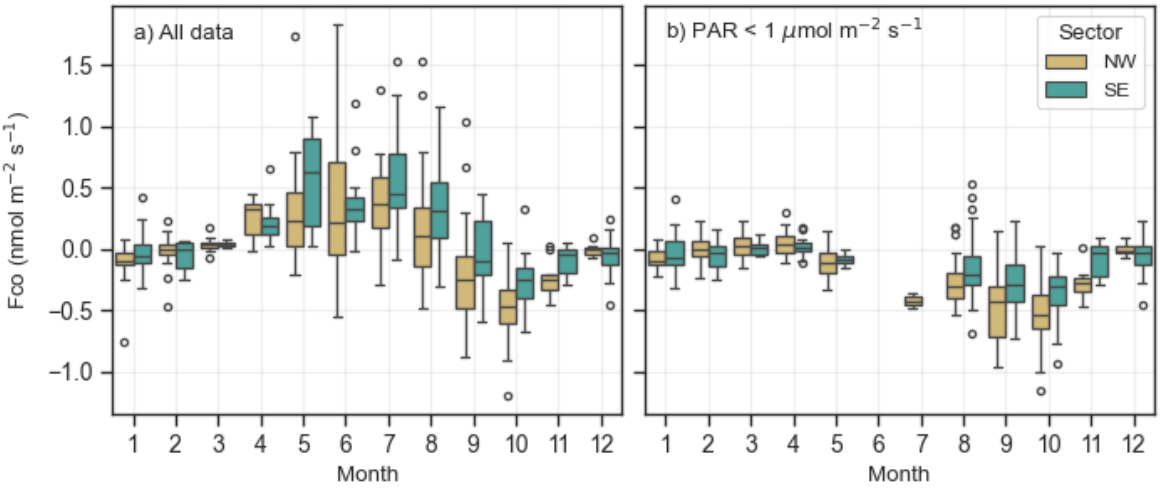

Figure 7. The boxplot of NW (yellow) and SE (turquoise) CO flux in different months a) all PAR levels and b) in dark conditions PAR <1 μmol m^{-2} s^{-1}. The box represents the interquartile range (IQR), with the lower limit at the 25th percentile and the upper limit at the 75th percentile, while the whiskers indicate the minimum and maximum values. Black dots represent outliers, defined as 1.5 × IQR.

Author contributions. A.L. and I.M. designed the study. A.L., I.M., E.L. and A.M. participated in the field measurements. A.B., K.M.K., I.M., M.P. contributed to data analysis and helped interpret the results. A.L. performed the data processing, data analysis and wrote the original draft. All authors contributed the reviewing and editing the final version.

Competing interests. The authors declare that they have no conflict of interest.

Acknowledgements. We acknowledge financial support from Research Council of Finland (NPERM project nr 341349, ICOS-FIRI), ICOS-FI via University of Helsinki funding, EU-INTERACT, the EU Horizon Europe ± Framework Programme for Research and Innovation (GreenFeedback nr. 101056921 and LiweFor nr. 101079192). We thank the Abisko Scientific Research Station and research infrastructures ICOS Sweden and SITES (both funded by the Swedish Research Council) for the support of the work done at the Abisko. Lastly, we acknowledge the use of Grammarly (https://www.grammarly.com/) and ChatGPT (https://chatgpt.com/) to check grammar and improve text clarity during the preparation of this manuscript.

References

Abisko Scientific Research Station: UAV - Digital Terrain Model from Stordalen Mire, 2024-06-12, Swedish Infrastructure for Ecosystem Science (SITES) Spectral, 2025a.

Abisko Scientific Research Station: UAV - RGB orthomosaic from Stordalen Mire, 2024-06-12, Swedish Infrastructure for Ecosystem Science (SITES) Spectral, 2025b.

Akaike, H.: Maximum likelihood identification of Gaussian autoregressive moving average models, Biometrika, 60, 255–265, 1973.

Aubinet, M., Grelle, A., Ibrom, A., Rannik, Ü., Moncrieff, J., Foken, T., Kowalski, A., Martin, P., Berbigier, P., Bernhofer, C., Clement, R., Elbers, J., Granier, A., Grünwald, T., Morgenstern, K., Pilegaard, K., Rebmann, C., Snijders, W., Valentini, R., and Vesala, T.: Estimates of the Annual Net Carbon and Water Exchange of Forests: The EUROFLUX Methodology, in: Advances in ecological research, vol. 30, pp. 113–175, Elsevier, https://doi.org/https://doi.org/10.1016/S0065-2504(08)60018-5, 1999.

Aubinet, M., Vesala, T., and Papale, D.: Eddy covariance: a practical guide to measurement and data analysis, Springer Science & Business Media, 2012.

Bartholomew, G. and Alexander, M.: Microbial metabolism of carbon monoxide in culture and in soil, Applied and Environmental Microbiology, 37, 932–937, 1979.

Bruhn, D., Albert, K. R., Mikkelsen, T. N., and Ambus, P.: UV-induced carbon monoxide emission from living vegetation, Biogeosciences, 10, 7877–7882, https://doi.org/10.5194/bg-10-7877-2013, 2013.

Buzacott, A. J., van den Berg, M., Kruijt, B., Pijlman, J., Fritz, C., Wintjen, P., and van der Velde, Y.: A Bayesian inference approach to determine experimental Typha latifolia paludiculture greenhouse gas exchange measured with eddy covariance, Agricultural and Forest Meteorology, 356, 110 179, 2024.

Conrad, R. and Seiler, W.: Role of microorganisms in the consumption and production of atmospheric carbon monoxide by soil, Applied and Environmental Microbiology, 40, 437–445, 1980.

Constant, P., Poissant, L., and Villemur, R.: Annual hydrogen, carbon monoxide and carbon dioxide concentrations and surface to air exchanges in a rural area (Québec, Canada), Atmospheric Environment, 42, 5090–5100, 2008.

Cordero, P. R., Bayly, K., Man Leung, P., Huang, C., Islam, Z. F., Schittenhelm, R. B., King, G. M., and Greening, C.: Atmospheric carbon monoxide oxidation is a widespread mechanism supporting microbial survival, The ISME journal, 13, 2868–2881, 2019.

Cowan, N., Helfter, C., Langford, B., Coyle, M., Levy, P., Moxley, J., Simmons, I., Leeson, S., Nemitz, E., and Skiba, U.: Seasonal fluxes of carbon monoxide from an intensively grazed grassland in Scotland, Atmospheric Environment, 194, 170–178, https://doi.org/https://doi.org/10.1016/j.atmosenv.2018.09.039, 2018.

Daniel, J. S. and Solomon, S.: On the climate forcing of carbon monoxide, Journal of Geophysical Research: Atmospheres, 103, 13 249–13 260, https://doi.org/https://doi.org/10.1029/98JD00822, 1998.

Derendorp, L., Quist, J., Holzinger, R., and Röckmann, T.: Emissions of H2 and CO from leaf litter of Sequoiadendron giganteum, and their dependence on UV radiation and temperature, Atmospheric environment, 45, 7520–7524, 2011.

Fraser, W. T., Blei, E., Fry, S. C., Newman, M. F., Reay, D. S., Smith, K. A., and McLeod, A. R.: Emission of methane, carbon monoxide, carbon dioxide and short-chain hydrocarbons from vegetation foliage under ultraviolet irradiation, Plant, cell & environment, 38, 980–989, 2015.

Funk, D. W., Pullman, E. R., Peterson, K. M., Crill, P. M., and Billings, W. D.: Influence of water table on carbon dioxide, carbon monoxide, and methane fluxes from Taiga Bog microcosms, Global Biogeochemical Cycles, 8, 271–278, https://doi.org/https://doi.org/10.1029/94GB01229, 1994.

Guenther, A., Jiang, X., Heald, C. L., Sakulyanontvittaya, T., Duhl, T. a., Emmons, L., and Wang, X.: The Model of Emissions of Gases and Aerosols from Nature version 2.1 (MEGAN2. 1): an extended and updated framework for modeling biogenic emissions, Geoscientific Model Development, 5, 1471–1492, 2012.

Inman, R. E., Ingersoll, R. B., and Levy, E. A.: Soil: a natural sink for carbon monoxide, Science, 172, 1229–1231, 1971.

Kaimal, J. C. and Finnigan, J. J.: Atmospheric boundary layer flows: their structure and measurement, Oxford university press, 1994.

King, G.: Attributes of atmospheric carbon monoxide oxidation by Maine forest soils, Applied and Environmental Microbiology, 65, 5257–5264, 1999.

King, G. M.: Land use impacts on atmospheric carbon monoxide consumption by soils, Global biogeochemical cycles, 14, 1161–1172, 2000.

King, G. M. and Weber, C. F.: Distribution, diversity and ecology of aerobic CO-oxidizing bacteria, Nature Reviews Microbiology, 5, 107–118, 2007.

King, J. Y., Brandt, L. A., and Adair, E. C.: Shedding light on plant litter decomposition: advances, implications and new directions in understanding the role of photodegradation, Biogeochemistry, 111, 57–81, 2012.

Kisselle, K. W., Zepp, R. G., Burke, R. A., de Siqueira Pinto, A., Bustamante, M. M., Opsahl, S., Varella, R. F., and Viana, L. T.: Seasonal soil fluxes of carbon monoxide in burned and unburned Brazilian savannas, Journal of Geophysical Research: Atmospheres, 107, LBA–18, 2002.

Kljun, N., Calanca, P., Rotach, M., and Schmid, H. P.: A simple two-dimensional parameterisation for Flux Footprint Prediction (FFP), Geoscientific Model Development, 8, 3695–3713, 2015.

Kohonen, K.-M., Kolari, P., Kooijmans, L. M. J., Chen, H., Seibt, U., Sun, W., and Mammarella, I.: Towards standardized processing of eddy covariance flux measurements of carbonyl sulfide, Atmospheric Measurement Techniques, 13, 3957–3975, https://doi.org/10.5194/amt-13-3957-2020, 2020.

Łakomiec, P., Holst, J., Friborg, T., Crill, P., Rakos, N., Kljun, N., Olsson, P.-O., Eklundh, L., Persson, A., and Rinne, J.: Field-scale CH_4 emission at a subarctic mire with heterogeneous permafrost thaw status, Biogeosciences, 18, 5811–5830, https://doi.org/10.5194/bg-18-5811-2021, 2021.

Lee, H., Rahn, T., and Throop, H.: An accounting of C-based trace gas release during abiotic plant litter degradation, Global Change Biology, 18, 1185–1195, 2012.

Lelieveld, J., Gromov, S., Pozzer, A., and Taraborrelli, D.: Global tropospheric hydroxyl distribution, budget and reactivity, Atmospheric Chemistry and Physics, 16, 12 477–12 493, 2016.

Liu, L., Zhuang, Q., Zhu, Q., Liu, S., Van Asperen, H., and Pihlatie, M.: Global soil consumption of atmospheric carbon monoxide: an analysis using a process-based biogeochemistry model, Atmospheric Chemistry and Physics, 18, 7913–7931, 2018.

Ludwig, S. M., Schiferl, L., Hung, J., Natali, S. M., and Commane, R.: Resolving heterogeneous fluxes from tundra halves the growing season carbon budget, Biogeosciences, 21, 1301–1321, https://doi.org/10.5194/bg-21-1301-2024, 2024.

Lundin, E., Crill, P., Grudd, H., Holst, J., Kristoffersson, A., Meire, A., Mölder, M., and Rakos, N.: ETC L2 Meteo, Abisko-Stordalen Palsa Bog, 2021-12-31–2023-08-31, https://hdl.handle.net/11676/7FmuhOKAOTvnJD1fZxjYMduv, 2023.

Malmer, N., Johansson, T., Olsrud, M., and Christensen, T. R.: Vegetation, climatic changes and net carbon sequestration in a North-Scandinavian subarctic mire over 30 years, Global Change Biology, 11, 1895–1909, https://doi.org/https://doi.org/10.1111/j.1365-2486.2005.01042.x, 2005.

Mammarella, I., Peltola, O., Nordbo, A., Järvi, L., and Rannik, Ü.: Quantifying the uncertainty of eddy covariance fluxes due to the use of different software packages and combinations of processing steps in two contrasting ecosystems, Atmospheric Measurement Techniques, 9, 4915–4933, 2016.

Mauder, M. and Foken, T.: Impact of post-field data processing on eddy covariance flux estimates and energy balance closure, Meteorologische Zeitschrift, 15, 597–610, 2006.

Moxley, J. and Smith, K.: Factors affecting utilisation of atmospheric CO by soils, Soil Biology and Biochemistry, 30, 65–79, 1998.

Muller, J. D., Qubaja, R., Koh, E., Stern, R., Bohak, Y. L., Tatarinov, F., Rotenberg, E., and Yakir, D.: Leaf carbon monoxide emissions under different drought, heat, and light conditions in the field, New Phytologist, 245, 2439–2450, 2025.

Murphy, R., Lanigan, G., Martin, D., and Cowan, N.: Carbon monoxide fluxes measured using the eddy covariance method from an intensively managed grassland in Ireland, Environmental Science: Atmospheres, 3, 1834–1846, 2023.

Pihlatie, M., Rannik, U., Haapanala, S., Peltola, O., Shurpali, N., Martikainen, P. J., Lind, S., Hyvönen, N., Virkajärvi, P., Zahniser, M., and Mammarella, I.: Seasonal and diurnal variation in CO fluxes from an agricultural bioenergy crop, Biogeosciences, 13, 5471–5485, https://doi.org/10.5194/bg-13-5471-2016, 2016.

Potter, C. S., Klooster, S. A., and Chatfield, R. B.: Consumption and production of carbon monoxide in soils: a global model analysis of spatial and seasonal variation, Chemosphere, 33, 1175–1193, 1996.

Ragsdale, S. W.: Life with carbon monoxide, Critical reviews in biochemistry and molecular biology, 39, 165–195, 2004.

Rannik, Ü. and Vesala, T.: Autoregressive filtering versus linear detrending in estimation of fluxes by the eddy covariance method, Boundary-Layer Meteorology, 91, 259–280, 1999.

Rich, J. J. and King, G.: Carbon monoxide consumption and production by wetland peats, FEMS Microbiology Ecology, 28, 215–224, https://doi.org/10.1111/j.1574-6941.1999.tb00577.x, 1999.

SMHI: Dataseries with normal values for the period 1991-2020, https://www.smhi.se/data/temperatur-och-vind/temperatur/dataserier-med-normalvarden-for-perioden-1991-2020, last access: 2025-03-05, 2024.

Stein, O., Schultz, M. G., Bouarar, I., Clark, H., Huijnen, V., Gaudel, A., George, M., and Clerbaux, C.: On the wintertime low bias of Northern Hemisphere carbon monoxide found in global model simulations, Atmospheric chemistry and physics, 14, 9295–9316, 2014.

Sun, W., Kooijmans, L. M., Maseyk, K., Chen, H., Mammarella, I., Vesala, T., Levula, J., Keskinen, H., and Seibt, U.: Soil fluxes of carbonyl sulfide (COS), carbon monoxide, and carbon dioxide in a boreal forest in southern Finland, Atmospheric Chemistry and Physics, 18, 1363–1378, 2018.

Szopa, S., Naik, V., Adhikary, B., Artaxo, P., Berntsen, T., Collins, W., Fuzzi, S., Gallardo, L., Kiendler-Scharr, A., Klimont, Z., H. Liao, N. U., and Zanis, P.: Short-lived Climate Forcers, p. 817–922, Cambridge University Press, 2021.

Tarr, M. A., Miller, W. L., and Zepp, R. G.: Direct carbon monoxide photoproduction from plant matter, Journal of Geophysical Research: Atmospheres, 100, 11 403–11 413, 1995.

Tikkasalo, O.-P., Peltola, O., Alekseychik, P., Heikkinen, J., Launiainen, S., Lehtonen, A., Li, Q., Martínez-García, E., Peltoniemi, M., Salovaara, P., Tuominen, V., and Mäkipää, R.: Eddy-covariance fluxes of CO_2, CH_4 and N_2O in a drained peatland forest after clear-cutting, Biogeosciences, 22, 1277–1300, https://doi.org/10.5194/bg-22-1277-2025, 2025.

Van Asperen, H., Warneke, T., Sabbatini, S., Nicolini, G., Papale, D., and Notholt, J.: The role of photo-and thermal degradation for CO 2 and CO fluxes in an arid ecosystem, Biogeosciences, 12, 4161–4174, 2015.

van Asperen, H., Warneke, T., Carioca de Araújo, A., Forsberg, B., José Filgueiras Ferreira, S., Röckmann, T., van der Veen, C., Bulthuis, S., Ramos de Oliveira, L., de Lima Xavier, T., et al.: The emission of CO from tropical rainforest soils, Biogeosciences, 21, 3183–3199, 2024.

Varella, R., Bustamante, M., Pinto, A., Kisselle, K., Santos, R., Burke, R., Zepp, R., and Viana, L.: Soil fluxes of CO2, CO, NO, and N2O from an old pasture and from native savanna in Brazil, Ecological Applications, 14, 221–231, 2004.

Varner, R. K., Crill, P. M., Frolking, S., McCalley, C. K., Burke, S. A., Chanton, J. P., Holmes, M. E., Coordinators, I. P., Saleska, S., and Palace, M. W.: Permafrost thaw driven changes in hydrology and vegetation cover increase trace gas emissions and climate forcing in Stordalen Mire from 1970 to 2014, Philosophical Transactions of the Royal Society A, 380, 20210 022, 2022.

Wang, M. and Liao, W.: Carbon monoxide as a signaling molecule in plants, Frontiers in Plant Science, 7, 572, 2016.

Whalen, S. and Reeburgh, W.: Carbon monoxide consumption in upland boreal forest soils, Soil Biology and Biochemistry, 33, 1329–1338, 2001.

Zheng, B., Chevallier, F., Yin, Y., Ciais, P., Fortems-Cheiney, A., Deeter, M. N., Parker, R. J., Wang, Y., Worden, H. M., and Zhao, Y.: Global atmospheric carbon monoxide budget 2000–2017 inferred from multi-species atmospheric inversions, Earth System Science Data, 11, 1411–1436, https://doi.org/10.5194/essd-11-1411-2019, 2019.